Optical fiber interferometer for measuring the *in situ* deflection characteristics of microelectromechanical structures

Tristan J. Tayag, MEMBER SPIE
Edward S. Kolesar
Brandon D. Pitt
Texas Christian University
Department of Engineering
TCU Box 298640
Fort Worth, Texas 76129
E-mail: t.tayag@tcu.edu

Kam See Hoon
Nanyang Polytechnic
School of Engineering
180 Ang Mo Kio Avenue 8
Singapore 569830

James Marchetti
Ijaz H. Jafri
Corning IntelliSense
36 Jonspin Road
Wilmington, MA 01887

Abstract. An optical fiber interferometer is described for measuring the out-of-plane displacement of microelectromechanical structures. The interferometric system has a theoretical measurement dynamic range greater than 10^8. Experimental results characterizing an electrostatically actuated polysilicon flexure beam are presented. The results are in good agreement with modeling data based on coupled boundary-element and finite-element analysis. *© 2003 Society of Photo-Optical Instrumentation Engineers.*
[DOI: 10.1117/1.1525275]

Subject terms: fiber optic interferometry; microelectromechanical systems (MEMS); finite-element analysis (FEA); boundary-element analysis (BEA).

Paper 020041 received Feb. 7, 2002; revised manuscript received Jun. 14, 2002; accepted for publication Jun. 14, 2002.

1 Introduction

The rapidly expanding field of microelectromechanical systems (MEMS) is experiencing phenomenal growth in communication and sensing applications. MEMS structures commercially available or under development for optical communication applications include optical crossconnects,[1] add-drop wavelength multiplexers,[2] gain equalizers,[3] and tunable lasers[4] and filters.[5] On the other hand, MEMS sensing applications have achieved commercial success in microaccelerometers.[6] Other MEMS sensors currently under investigation include pressure sensors,[7] magnetic field sensors,[8] resonant transducer sensors,[9] and gyroscopic sensors.[10] Although not all MEMS structures involve movable components, the devices listed here share the common trait that they include some out-of-plane movable component.

To develop viable MEMS devices for these applications, a noninvasive system for characterizing out-of-plane displacements as a function of the actuation parameter(s) is desirable. As an added benefit, the measured data frequently can be used to deduce material property information. Information of this type provides feedback for adjusting the fabrication and processing conditions to achieve optimal device performance. With respect to device development, it is also important that the sensing system be capable of *in situ* characterization. In this context, it is desirable that the system be sufficiently flexible to make measurements on MEMS devices mounted on a probe station or at the wafer level during process development and manufacturing.[11]

The length scale of out-of-plane motion typically ranges from subnanometer to several microns of displacement. The fine resolution and wide dynamic range afforded by optical detection techniques provides a good match with the demands of MEMS measurements. As a result, several optical systems have been developed for measuring the out-of-plane displacement of MEMS structures. These optical techniques may be broadly categorized as interferometric and noninterferometric. Noninterferometric techniques typically modulate the power coupled into an optical fiber so that it is proportional to the displacement of the MEMS device. These techniques include the optical beam deflection method,[12] the shutter method, and the lever method.[13]

Interferometric techniques can be categorized as single-point measurement techniques and full-field optical measurement techniques. Single-point methods measure the transverse displacement at a single point on the MEMS structure. Both bulk optical[14] and fiber optic[15] interferometers have been used to characterize the displacement at specific points on the MEMS device. These approaches may be scanned to yield linear or two-dimensional displacement data.[16] Full-field optical measurement techniques have been applied to MEMS structures, and they include holographic interferometry,[17,18] moiré interferometry[18] and stroboscopic interferometry.[19]

In contrast with sensing systems applied strictly for the development of MEMS devices, some sensor systems are integrated as part of the overall system architecture. Detection mechanisms used with MEMS sensors include electrostatic, piezoelectric, magnetic, piezoresistive, and optical.[20] In this paper, we confine ourselves to detection schemes based on optical methods. Both integrated optical[21,22] and fiber optic[23,24] approaches for characterizing MEMS sensors have been investigated. Since the fiber optic sensing schemes are not inherently tied to the MEMS structure,

 © 2003 Society of Photo-Optical Instrumentation Engineers

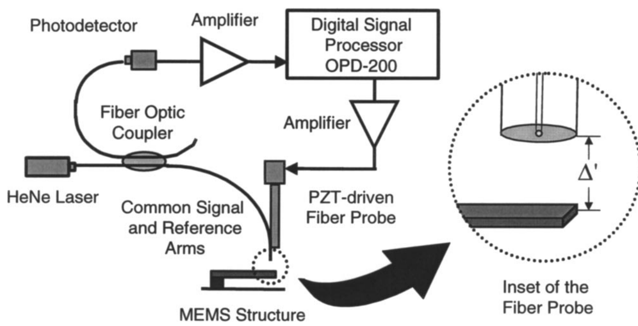

Fig. 1 Interferometric system.

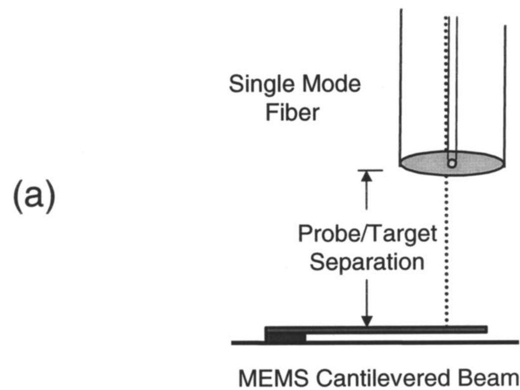

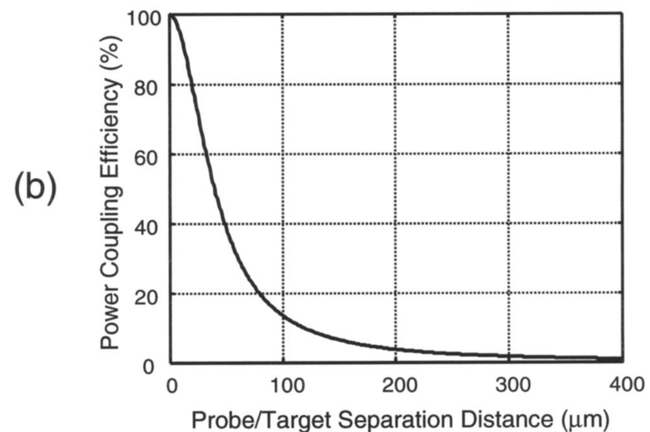

Fig. 2 Analysis of the power coupling efficiency of the fiber probe, showing (a) the geometry of the system and (b) the power coupling efficiency versus probe-to- target separation distance at zero tilt of the fiber axis with respect to the target normal.

they are amenable to the more general application of *in situ* MEMS characterization.

In this paper, an optical fiber interferometer is described for measuring the *in situ* deflection characteristics of MEMS structures. Common signal and reference beam paths, together with digital demodulation techniques, provide a robust sensing system, which is tolerant of angular misalignments of the fiber probe. The system can be expanded to multiple sensor heads for the interrogation of different elements in a MEMS device. To our knowledge, this is the first time this interferometric system has been applied to the *in situ* characterization of MEMS structures. In Sec. 2, the interferometer is described with respect to its optical configuration and digital demodulation technique. The operational characteristics of this system are analyzed in terms of its dynamic range of measurement and its range of operating frequencies. In Sec. 3, experimental results for the characterization of a MEMS electrostatically deflectable beam are presented. The well-known polysilicon MEMS cantilever beam was chosen as the test structure so that mature modeling techniques could be used to validate the system response. In Sec. 4 is the conclusion.

2 Fiber Interferometer

2.1 *System Configuration*

The interferometer system configuration is shown in Fig. 1. Polarized light with a wavelength of 0.6328 μm is coupled into a single-mode optical fiber. The light is then split with a 3-dB fused fiber coupler. One of the output pigtails of the coupler is attached to a piezoelectric transducer stack [made from lead zirconate titanate (PZT)], which moves the tip of the fiber along the axis of the fiber. This pigtail serves as the fiber probe of the interferometer. The coupler's other pigtail is unused. It is immersed in index-matching fluid to minimize back reflections.

The tip of the fiber probe is cleaved so that the normal to the cleaved fiber facet is collinear with the fiber axis. The cleaved facet serves as both the interferometer's beamsplitter and its beam combiner. The air-fiber interface at the cleaved facet of the fiber probe provides 4% power reflection back into the single-mode fiber. This reflected field is the interferometer's reference beam. The light transmitted through the fiber probe's facet reflects off the MEMS structure to be measured and is coupled back into the fiber. Consequently, the cleaved facet now acts as a beam combiner. The round-trip distance traveled out of the fiber, off the MEMS structure, and back into the fiber forms the signal path of the interferometer. The reference and signal fields copropagate back through the fiber until they reach the fused fiber coupler, where an additional 3-dB power reduction is encountered. Finally, the interference signal is detected with a photodetector.

The efficiency of coupling of the signal field back into the fiber probe is a critical feature of this interferometer configuration. We have modeled the coupling efficiency of the fiber probe, assuming Gaussian field propagation out of the fiber and reflection off a tilted specular surface. The power coupling efficiency versus the probe-to-target separation distance is plotted in Fig. 2. Given zero tilt of the fiber probe with respect to the target surface normal, the probe-to-target separation distance must be less than 195 μm for greater than 4% power coupling of the signal field back into the fiber.

Figure 3 shows the power coupling efficiency versus probe tilt angle at a separation distance of 100 μm. From an implementation perspective, high tolerance to angular misalignment of the probe is desired. The bare fiber probe tolerates approximately ± 4 deg of misalignment at a separation distance of 100 μm. This limitation is sufficient for the *in situ* characterization of MEMS structures.

The optical configuration described above has been used with varying demodulation schemes to characterize MEMS sensors,[15] hard disk surfaces,[25] and biological

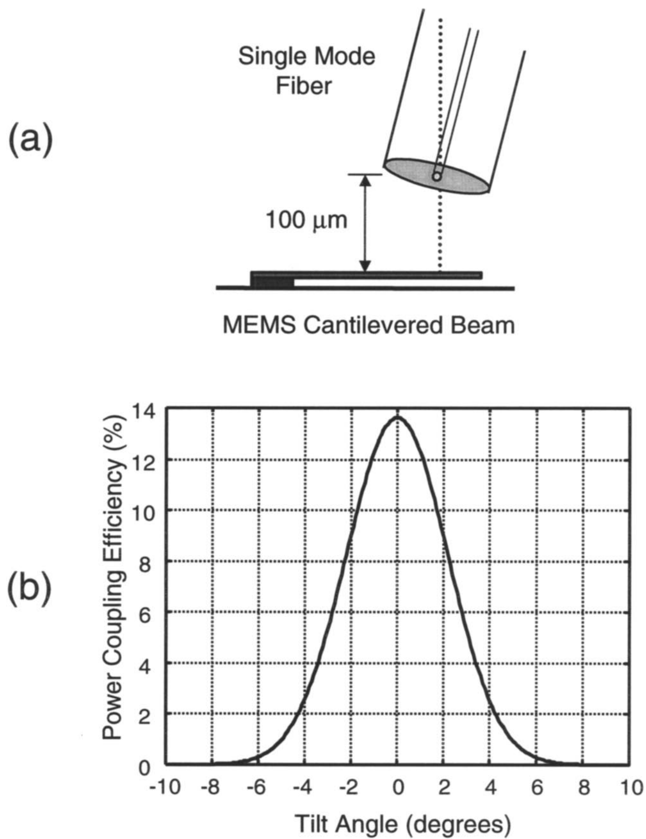

Fig. 3 Analysis of the power coupling efficiency of the fiber probe, showing (a) the geometry of the system and (b) the power coupling efficiency versus tilt angle of the fiber axis with respect to the target normal at a separation distance of 100 μm.

membranes.[26] The common signal and reference paths in this optical configuration eliminate signal fading due to non-signal-induced polarization drift and optical-path-length drift in the fiber. Also, the common signal and reference paths obviate the need for high-cost polarization-preserving single-mode fiber.

Demodulation of the optical signal is implemented by sampling the photodetected signal and performing digital signal processing on it. The OPD-200 digital demodulator is a commercially available instrument from Optiphase™, Inc., which was used to perform the digital demodulation.[27] The demodulation algorithm is based on a passive homodyne scheme using a phase-generated carrier.[28] In our interferometer, the phase-generated carrier is imposed on the signal by modulating the open-air signal path between the fiber probe and the MEMS structure.

We verified the digital demodulation of the fiber interferometer by comparing the phase output from the OPD-200 with a direct measurement of the phase. A PZT-mounted mirror was used in place of the MEMS structure in Fig. 1. The mirror was vibrated sinusoidally at 1 kHz with varying drive voltages applied to its PZT stack. The direct measurement of the mirror motion was obtained by noting that at integer multiples of 2π rad in the interferometer's optical path difference, characteristic waveforms are produced by the interfering beams. For example, the bottom trace in Fig. 4 illustrates the photodetected waveform

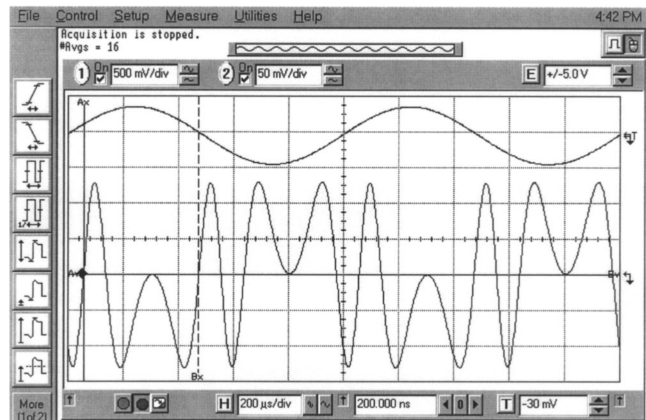

Fig. 4 Interferometric measurement of a PZT-driven mirror. The upper oscilloscope trace is the signal driving the PZT-mounted mirror, and the lower trace is the amplified output signal from the photodetector. The output signal exhibits the characteristic waveform for a 4π phase shift.

for a 4π-rad optical-path-length difference. Direct measurement data corresponding to optical-path-length differences of 2π and 4π versus the voltage applied to the PZT stack are plotted as $\times$'s in Fig. 5. Agreement between the direct measurement result and the demodulation output from the OPD-200 (plotted as ○'s) is evident in Fig. 5.

2.2 *System Dynamic Range*

The displacement measurement and frequency response of the interferometer system described above have a large dynamic range. The digital demodulation technique facilitates both fractional-fringe and fringe-counting interrogation of the interferometric signal. This technique has a theoretical dynamic range greater than 10^8 for measuring surface displacements.

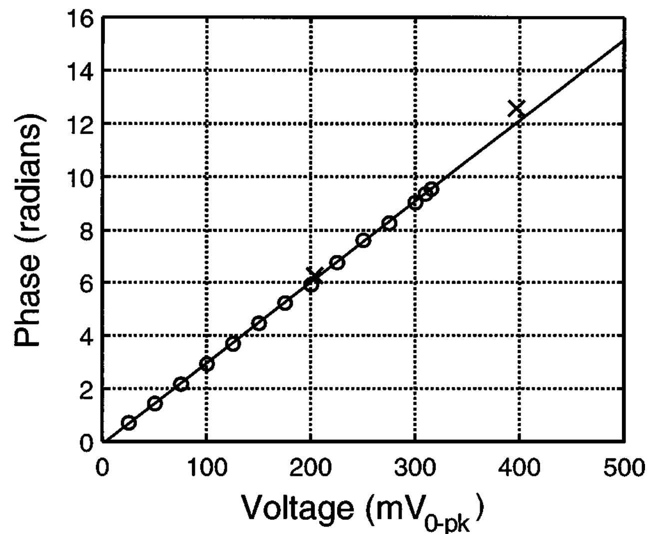

Fig. 5 Comparison of the OPD-200 digital demodulator output with a direct measurement of the interferometer's phase ($\times$, direct measurement data point; ○, OPD-200 data point; solid line, linear fit to the OPD-200 data).

The ultimate system resolution of a displacement-measuring interferometer refers to a limit on the system's ability to detect surface changes. This limit is expressed in terms of the smallest displacement that can be detected if the signal-to-noise ratio (SNR) is unity.[29] Photodetector quantum noise and analog-to-digital converter quantization noise are examples of noise sources that cannot be eliminated from the system. In the present system, the detector quantum noise (also called shot noise) sets the limit to the ultimate performance of the interferometric system. We have determined the quantum-noise-limited sensitivity of the interferometer shown in Fig. 1 to be 24 pm.[30]

The degree to which this ultimate resolution may be achieved depends on numerous factors. The foremost consideration for this interferometer configuration is the field contrast ratio. In practice, it is very difficult to secure a unity field contrast ratio. For values of field contrast not equal to one, the fringe contrast and the SNR decrease, thereby increasing the minimum detectable displacement. In practice, we have achieved a system resolution of several nanometers.

The number of bits in the digital demodulator that are used to keep the fringe count limits the full measurement range of the interferometer. This limitation places an upper bound of 2.6 mm on the measurement range. In practice, however, an increased separation distance between the fiber probe and the MEMS structure results in decreased efficiency of coupling into the fiber and loss of optical signal. Davis et al.[25] have shown that the OPD-200 digital demodulator is capable of performing demodulation with low signal levels. With an operating wavelength of 1.55 μm, they have characterized hard-disk surfaces with displacements greater than 350 μm. For our operating wavelength of 0.6328 μm, this corresponds to a displacement greater than 140 μm. The practical measurement range of several nanometers to more than 140 μm is well suited to the out-of-plane characterization of MEMS structures.

The interferometric system is capable of measuring displacements ranging in frequency from dc to one-half the frequency of the phase-generated carrier. The OPD-200 provides the drive signal for the phase-generated carrier and is capable of modulation rates up to 95 kHz. In our interferometric configuration, however, the PZT stack limits the modulation frequency. The PZT and drive electronics in our system limit the carrier frequency to 10 kHz. Therefore, our system is capable of measuring displacements ranging from dc to 5 kHz.

3 Characterization of a MEMS Flexure Beam

A MEMS flexure beam is a clamped-free cantilever beam, where a small section of the beam material near the base of the post has been removed to produce a hinge point on the beam (see Fig. 6). Polysilicon flexure beams with dimensions given in Fig. 6 were fabricated via the Multi-User MEMS Processes (MUMPs®) foundry service available from JDS Uniphase.[31] We used the fiber interferometer to measure the transverse deflection of the flexure beam under electrostatic actuation. Additionally, we simulated the motion of the flexure beam using a coupled boundary-element analysis (BEA) and finite-element analysis (FEA) software tool (IntelliSuite™ Windows NT Version 5.1) available from Corning IntelliSense. In the coupled approach, BEA uses a surface mesh and solves the electrostatic aspect of the problem, while FEA uses a volume mesh and solves the mechanical aspect of the problem. When considering electrostatically actuated devices, the coupled approach tends to several advantages over a pure finite-element approach, including faster simulation times and higher accuracy.

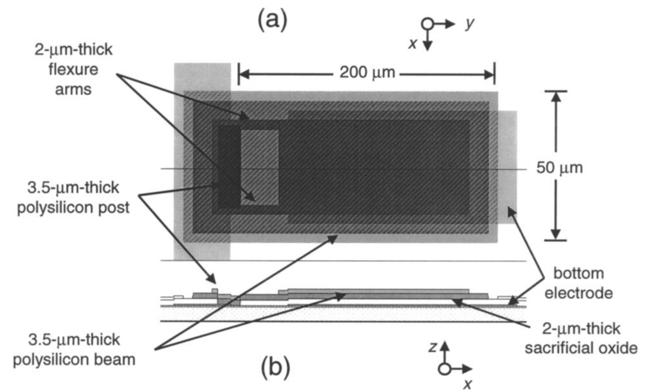

Fig. 6 Geometry of a MEMS flexure beam showing (a) the top view and (b) the side view.

The flexure beam was electrostatically excited into transverse motion with the application of a 2.5-V (zero to peak) sinusoid oscillating at 1 kHz. An example of the interferometer's measurement is shown in Fig. 7. Channel 1 is the upper trace and shows the voltage signal driving the flexure beam. Channel 2 is the lower trace and shows the demodulation output from the OPD-200. Given the round-trip path taken by the signal beam in our interferometer configuration (see Fig. 1), the peak-to-peak deflection of the device under test may be described as

$$\Delta l_{\mathrm{pk-pk}} = \frac{\lambda\ \Delta \phi}{4\pi},$$

where $\Delta\phi$ is the phase difference between the signal and reference beams. The digital demodulator scale is set to 0.5 rad/V, which corresponds to a peak-to-peak beam deflection of 5.5nm.

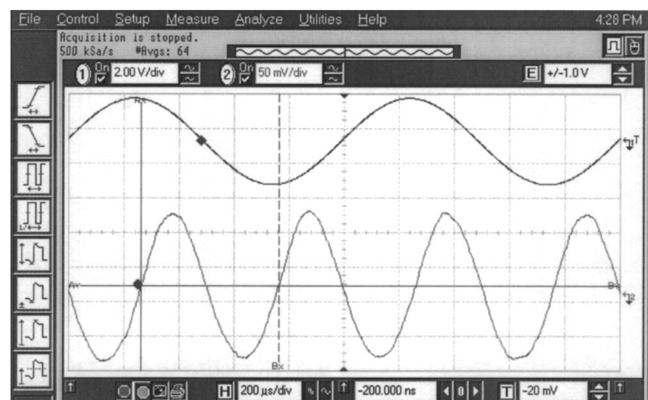

Fig. 7 Interferometric measurement of a MEMS flexure beam. The upper oscilloscope trace is the signal driving the MEMS structure, and the lower trace is the OPD-200 demodulator's output. The demodulated output signal scale corresponds to 25.18 nm/V.

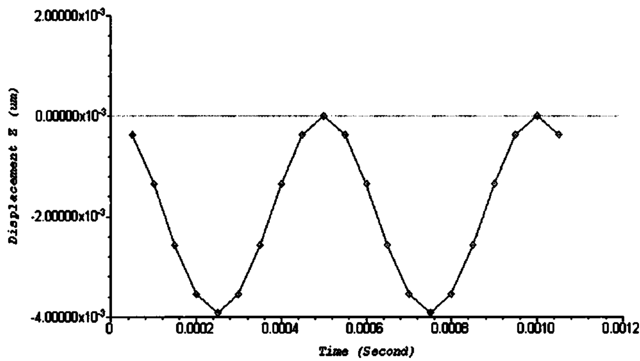

Fig. 8 Coupled boundary element analysis and finite element analysis simulation of a MEMS flexure beam. The signal driving the MEMS beam is 2.5 sin($2\pi\cdot 1000t$) V.

Figure 8 shows the numerical simulation of the flexure beam's deflection based upon the coupled BEA and FEA technique. The mesh size was 30 μm, and the following material properties were used for the polycrystalline silicon beam:

Young's modulus: 160 GPa

Density: 2.3 gm/cm^3

Poisson's ratio: 0.226

The data in Fig. 8 indicate that the flexure beam deflects toward the substrate with a frequency of 2 kHz and a peak-to-peak amplitude of 4.0 nm. This simulation result compares well with the experimental data.

Of particular interest is the oscillation frequency of the flexure beam. The demodulation output shown in the lower trace of Fig. 7 indicates that the flexure beam is oscillating at 2 kHz, or *twice* the excitation frequency. During the negative voltage portion of the excitation sinusoid's period [see Fig. 9(a)], the **E** field is in the $+z$ direction. The negative charge, $-Q$, accumulated on the beam's electrode experiences a force given by $\mathbf{F}=-Q\mathbf{E}$;so the beam is deflected towards the substrate. During the positive-voltage portion of the excitation sinusoid's period [see Fig. 9(b)], the **E** field is in the $-z$ direction. The positive charge, Q, accumulated on the beam's electrode experiences a force$\mathbf{F}=Q\mathbf{E}$; so the beam is again deflected towards the substrate.

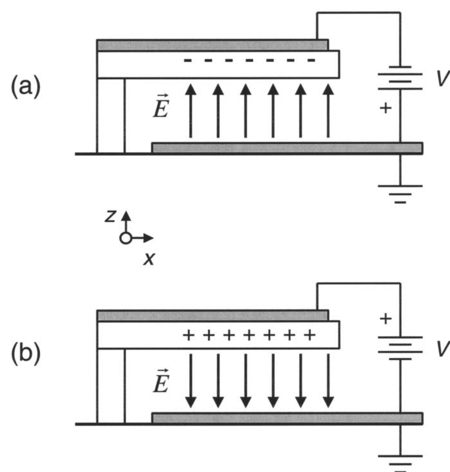

Fig. 9 Electrostatic attraction of a MEMS cantilever beam with (a) negative voltage applied to the beam and (b) positive voltage applied to the beam.

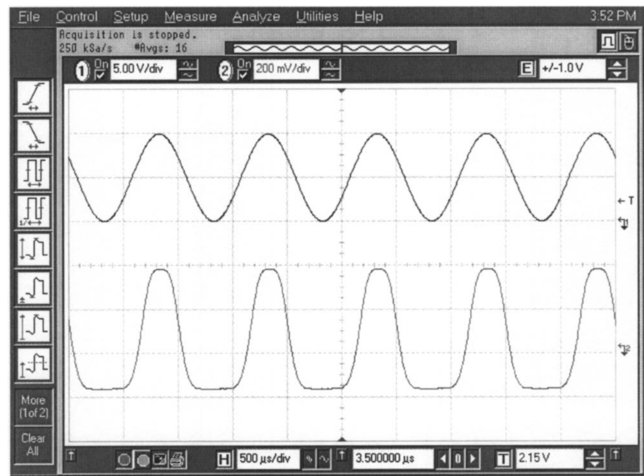

Fig. 10 Removal of the frequency-doubling effect. The upper oscilloscope trace is a biased excitation signal driving the MEMS structure, and the lower trace is the raw interferometer output signal prior to demodulation. The signal driving the MEMS beam is 5 +5 sin($2\pi\cdot 1000t$) V.

Electrostatically driven MEMS structures experience only electrostatic attraction (as opposed to electrostatic repulsion). Thus, for a bipolar excitation signal with zero mean, the oscillation frequency of the beam is twice that of the excitation signal. This frequency-doubling effect may be removed by adding a dc bias to the excitation signal such that the excitation signal is always a positive voltage or always a negative voltage. Figure 10 shows a biased excitation signal (upper trace) and the raw interferometer output signal prior to digital demodulation (lower trace). The excitation signal is $5+5\sin(2\pi\cdot 1000t)$ V. Note that both the excitation and the raw interferometer's response are oscillating at 1 kHz.

Two points of clarification are necessary with respect to the interferometer data displayed in Fig. 7. First, the interferometer measures relative phase shifts between a reference light wave and a signal light wave. The demodulator reads both the offset phase (representing the optical-path mismatch) and the dynamic signal created by the beam flexure. Therefore, a zero voltage reading at the demodulator output does not necessarily correspond to zero deflection. Second, an artifact of the digital demodulation scheme is a fixed time delay in the output data, which corresponds to the time for one demodulation cycle. For the modulation frequency used in Fig. 7, the delay is about 124 μs.

Finally, we measured the deflection at the tip of the flexure beam as a function of the excitation voltage at 1 kHz. As shown in Fig. 11, the experimentally measured data are in reasonably good agreement with the simulation data. However, a discrepancy in deflection amplitudes at the larger excitation voltages exists between the experimental and the simulation data. Further simulation results indicate that magnitude of this discrepancy is not attributable to

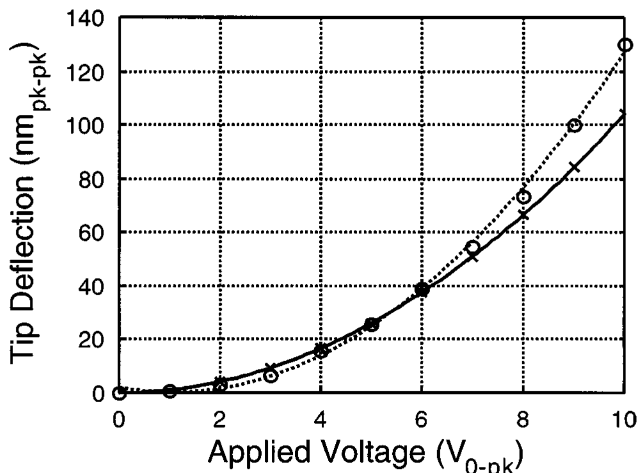

Fig. 11 Tip deflection of the MEMS flexure beam versus applied voltage at a frequency of 1 kHz (×, FEA simulation data point; solid curve, quadratic fit to the simulation data; ○, experimental data point; dotted curve, quadratic fit to the experimental data).

variations in the beam parameters (e.g., Young's modulus and beam length) or to the onset of spontaneous collapse of the flexure beam. Furthermore, simulation indicates that the flexure beam has a transverse mode resonance at 73 kHz. Our beam oscillation frequency of 2 kHz is sufficiently removed from resonance that overshoot of the beam cannot be the cause of the discrepancy. This discrepancy between the experiment and simulation is currently under investigation.

4 Summary

We have reported a fiber optic interferometer, which is suitable for the *in situ* characterization of MEMS structures. The optical configuration of the interferometer is robust with respect to environmental perturbations as well as to angular misalignment of the fiber probe. Commercially available digital signal-processing instrumentation is used to demodulate the interferometric signal. We determined that the theoretical dynamic range of the system is greater than 10^8.

We have applied this interferometer to measure the transverse deflection of a MEMS flexure beam. We investigated the response of the flexure beam to both bipolar and unipolar excitation sinusoids, and we characterized the tip deflection as a function of applied voltage. Our experimental results were in reasonably good agreement with coupled BEA and FEA simulation of the flexure beam.

Acknowledgments

This material is based upon work supported in part by the U.S. Army Research Laboratory and the U.S. Army Research Office under grant No. DAA655-98-1-0477. The authors thank Mr. David Yale for machining components for the interferometer.

References

1. D. T. Neilson and R. Ryf, "Scalable micromechanical optical cross-connects," *Proc. LEOS 2000* **1**, 48–49 (2000).
2. J. E. Ford, V. A. Aksyuk, D. J. Bishop, and J. A. Walker, "Wavelength add-drop switching using tilting mirrors," *J. Lightwave Technol.* **17**(5), 904–911 (1999).
3. J. E. Ford and J. A. Walker, "Dynamic spectral power equalization using micro-optomechanics," *IEEE Photonics Technol. Lett.* **10**(10), 1440–1442 (1998).
4. C. J. Chang-Hasnain, "Tunable VSCEL," *IEEE J. Sel. Top. Quantum Electron.* **6**(6), 978–981 (2000).
5. P. Tayebati, P. D. Wang, D. Vakhshoori, and R. N. Sacks, "Widely tunable Fabry-Perot filter using Ga(Al)As-AlO_x deformable mirrors," *IEEE Photonics Technol. Lett.* **10**(3), 394–396 (1998).
6. C. Burrer, J. Esteve, and E. Lora-Tamayo, "Resonant silicon accelerometers in bulk micromachining technology—an approach," *J. Microelectromech. Syst.* **5**(2), 122–130 (1996).
7. H. Porte, V. Gorel, S. Kiryenko, J. P. Goedgebuer, W. Daniau, and P. Blind, "Imbalanced Mach-Zehnder interferometer integrated in micromachined silicon substrate for pressure sensor," *J. Lightwave Technol.* **17**(2), 229–233 (1999).
8. Z. Kadar, A. Bossche, and J. Mollinger, "Integrated resonant magnetic-field sensor," *Sens. Actuators A* **41–42**, 66–69 (1994).
9. G. Stemme, "Resonant silicon sensors," *J. Micromech. Microeng.* **1**, 113–125 (1991).
10. G. T. A. Kovacs, "Micromachined gyroscopes," Sec. 5.2.3 in *Micromachined Transducers Sourcebook*, pp. 242–248, McGraw-Hill, Boston (1998).
11. P. M. Osterberg and S. D. Senturia, "M-TEST: A test chip for MEMS material property measurement using electrostatically actuated test structures," *J. Microelectromech. Syst.* **6**(2), 107–117 (1997).
12. J. W. Shin, S.W. Chung, Y. K. Kim, and B. K. Choi, "Design and fabrication of micromirror array support by vertical springs," *Sens. Actuators A* **66**, 144–149 (1998).
13. G. He and F. W. Cuomo, "Displacement response, detection limit, and dynamic range of fiber optic level sensors," *J. Lightwave Technol.* **9**(11), 1618–1625 (1991).
14. F. Lärmer, A. Schilp, K. Funk, and C. Burrer, "Experimental characterization of dynamic micromechanical transducers," *J. Micromech. Microeng.* **6**, 177–186 (1996).
15. A. Gutièrrez, D. Edmans, C. Cormeau, G. Seidler, D. Deangelis, and E. Maby, "Silicon micromachined sensor for broadband vibration analysis," in *Proc. Int. Conf. on Integrated Micro/Nanotechnology for Space Appl.*, NASA, Houston, TX (1995).
16. R. A. Lawton, M. Abraham, and E. Lawrence, "Characterization of non-planar motion in MEMS involving scanning laser interferometry," *Proc. SPIE* **3880**, 46–50 (1999).
17. W. Jüptner, M. Kujawinska, W. Osten, L. Salbut, and S. Seebacher, "Combined measurement of silicon microbeams by grating interferometry and digital holography" *Proc. SPIE* **3407**, 348–357 (1998).
18. G. Wernicke, O. Kruschke, N. Demoli, and H. Gruber, "Some investigations in holographic microscopic interferometry with respect to the estimation of stress and strain in micro-opto-electro-mechanical systems (MOEMS)," *Proc. SPIE* **3407**, 358–364 (1998).
19. M. Hart, R. Conant, K. Lau, and R. Muller, "Stroboscopic phase-shifting interferometry for dynamic characterization of optical MEMS," *Proc. SPIE* **3749**, 468–469 (1999).
20. A. Prak, T. S. J. Lammerink, and J. H. J. Fluitman, "Review of excitation and detection mechanisms for micromechanical resonators," *Sens. Mater.* **5**(3), 143–181 (1993).
21. P. Pliska and W. Lukosz, "Integrated-optical acoustical sensors," *Sens. Actuators A* **41–42**, 93–97 (1994).
22. H. Porte, V. Gorel, S. Kiryenko, J. P. Goedgebuer, W. Daniau, and P. Blind, "Imbalanced Mach-Zehnder interferometer integrated in micromachined silicon substrate for pressure sensor," *J. Lightwave Technol.* **17**(2), 229–233 (1999).
23. D. S. Greywall, "Micromechanical light modulators, pressure gauges, and thermometers attached to optical fibers," *J. Micromech. Microeng.* **7**, 343–352 (1997).
24. O. Tohyama, M. Kohashi, M. Sugihara, and H. Itoh, "A fiber-optic pressure microsensor for biomedical applications," *Sens. Actuators A* **66**, 150–154 (1998).
25. P. G. Davis, I. J. Bush, and G. S. Maurer, "Fiber optic displacement sensor," *Proc. SPIE* **3489**, 18–22 (1998).
26. A. D. Drake and D. C. Leiner, "A fiber Fizeau interferometer for measuring minute biological displacements," *IEEE Trans. Biomed. Eng.* **BME-31**(7), 507–511 (1984).
27. A. Cekorich, "Demodulator for interferometric sensors," *Proc. SPIE* **3860**, 338–347 (1999).
28. A. Dandridge, A. B. Tveten, and T. G. Giallorenzi, "Homodyne demodulation scheme for fiber optic sensors using phase generated carrier," *IEEE J. Quantum Electron.* **QE-18**(10), 1647–1653 (1982).
29. J. W. Wagner and J. B. Spicer, "Theoretical noise-limited sensitivity of classical interferometry," *J. Opt. Soc. Am. B* **4**(8), 1316–1326 (1987).
30. T. J. Tayag, "Quantum-noise-limited sensitivity of an interferometer using a phase generated carrier demodulation scheme," *Opt. Eng.* **41**(2), 276–277 (2002).
31. P. B. Allen, J. M. Wilken, and E. S. Kolesar, "Design, fabrication, and

performance evaluation of several electrical and mechanical silicon microstructures realized using the emerging technology of microelectromechanical systems (MEMS)," in *Proc. American Soc. Eng. Educ.*, Houston, TX, pp. 43–48 (1997).

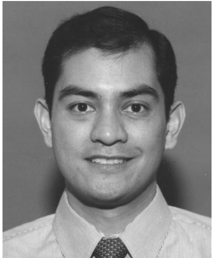

Tristan J. Tayag received his BSEE and MSE degrees from the Johns Hopkins University in 1986 and 1987, respectively, and his PhD degree from the University of Virginia in 1991. In 1986, he joined the Applied Physics Laboratory of the Johns Hopkins University, where he conducted research in fiber optic sensors for biomedical applications. From 1991 through 1997, he was engaged in the development of integrated optical signal processors at the U.S. Army Research Laboratory. He served as a visiting scientist at the U.S. Military Academy at West Point during the 1996 academic year. Currently, he is an associate professor at Texas Christian University, where his research interests include optical sensing, MEMS, and digital signal processing. He is a member of IEEE, OSA, and SPIE.

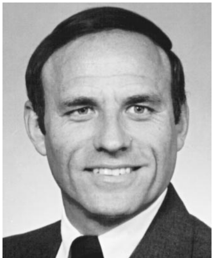

Edward S. Kolesar received his BSEE degree from The University of Akron in 1973, his MSEE degree from the Air Force Institute of Technology in 1978, and his PhD degree from The University of Texas at Austin in 1985. Before retiring with the rank of professor, he served on the faculty and as vice chair in the Department of Electrical and Computer Engineering at the Air Force Institute of Technology. There he initiated a microsensors and microtransducers research program while serving as the research advisor for more than 30 MS and PhD students. Upon retirement from the USAF in 1993 as a lieutenant colonel, he joined the faculty in the Department of Engineering at Texas Christian University, where he is the W. A. Moncrief Professor of Engineering. His current research interests include microelectromechanical systems (MEMS), silicon micromachined gas chromatography systems, and organic semiconductors. He holds 11 U.S. patents, and is the author of more than 100 refereed journal articles, book chapters and technical reports. He is a registered professional engineer in Texas; a member of Tau Beta Pi, Eta Kappa Nu, and Sigma Xi; and a senior member of the IEEE.

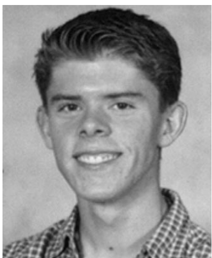

Brandon D. Pitt is a third-year undergraduate student studying engineering at Texas Christian University. He was recently awarded a 2002 SPIE Educational Scholarship in Optical Science and Engineering and a scholarship from the Instrumentation, Systems, and Automation Society. His research interests include MEMS modeling and digital signal processing.

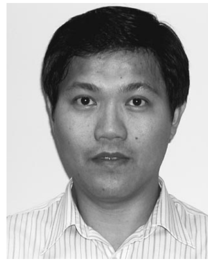

Kam See Hoon received his BEng(Hons) degree in electrical engineering from the National University of Singapore in 1990. He is presently an academic staff member with the School of Engineering, Nanyang Polytechnic, Singapore. His current research interest is in the design of MEMS devices for photonics and biomedical applications.

James Marchetti received his BS in chemical engineering from the Massachusetts Institute of Technology in 1996, where he completed a thesis focused on process optimization for biopharmaceutical manufacturing processes. James currently heads Corning IntelliSense's software business. With over six years of commercial experience in the CAD-for-MEMS market, he manages Corning IntelliSense's world-wide international distribution and commercial partnership channels, and serves as a liaison between IntelliSense and its customer base. He works with customers in the telecommunications and life-sciences industries on CAD-based device design, MEMS process simulation, and virtual prototyping. He is a member of Tau Beta Pi, Sigma Xi, and the American Institute of Chemical Engineering.

Ijaz H. Jafri received his BS from New York Institute of Technology, and his MS and PhD from State University of New York at Stony Brook (all in mechanical engineering). He holds five U.S. patents in semiconductor and MEMS technologies. He has numerous peer-reviewed journal and conference publications. Dr. Jafri has conducted research as principal investgator of various federal and private funded programs for developing new systems and technologies for III-V compound semiconductors, bulk polysilicon growth, purification of metallurgical grade silicon, critical-point drying for MEMS, and supercritical-fluid-based photoresist removal for the semiconductor industry. At Corning IntelliSense, as manager applications engineering, he conducts applied research and development in MEMS technology. His research interests in MEMS design and process include electrostatically and thermally actuated devices, micro hot-plate sensors, rf switches, microrelays, microswitches, micromirrors, stiction in MEMS, and microfluidics applications. He is an associate member of American Society of Mechanical Engineers.